

Magnetoacoustic tomography with magnetic induction for imaging electrical impedance of biological tissue

Xu Li, Yuan Xu, and Bin He^{a)}

Department of Biomedical Engineering, University of Minnesota, Minneapolis, Minnesota 55455

(Received 19 August 2005; accepted 17 February 2006; published online 29 March 2006)

An experimental feasibility study was conducted on magnetoacoustic tomography with magnetic induction (MAT-MI). It is demonstrated that the two-dimensional MAT-MI system can detect and image the boundaries between regions of different electrical conductivities with high spatial resolution. Utilizing a magnetic stimulation coil, MAT-MI evokes magnetically induced eddy current in an object which is placed in a static magnetic field. Because of the existence of Lorenz forces, the eddy current in turn causes acoustic vibrations, which are measured around the object in order to reconstruct the electrical impedance distribution of the object. The present experimental results from the saline and gel phantoms are promising and suggest the merits of MAT-MI in imaging electrical impedance of biological tissue with high spatial resolution. © 2006 American Institute of Physics. [DOI: 10.1063/1.2186371]

Magnetoacoustic tomography with magnetic induction (MAT-MI) is an imaging modality combining pulsed magnetic stimulation with sonography and it is proposed for imaging the electrical impedance of samples noninvasively.¹ Noninvasive measurement of electrical properties of biological tissue has drawn substantial research interest for decades and a variety of techniques has been developed such as electrical impedance tomography (EIT),²⁻⁴ magnetic resonance electrical impedance tomography (MREIT),⁵⁻⁷ and magnetic induction tomography (MIT).^{8,9} In addition, magnetoacoustic tomography^{10,11} (MAT) and Hall effect imaging^{12,13} (HEI) have both been reported for combining bioelectromagnetism together with sonography.

In the MAT-MI approach we investigated here, pulsed magnetic stimulation (microseconds) is imposed on an object placed in a static magnetic field. The magnetically induced eddy current is then subject to Lorenz force. The Lorenz force causes acoustic vibrations which can be measured to reconstruct the conductivity distribution of the sample. Denoting the static magnetic field as \mathbf{B}_0 , the magnetically induced current density distribution as $\tilde{\mathbf{J}}$ (the tilt over a variable indicates a function of time; otherwise, the variable is not a function of time if not denoted explicitly), the Lorenz force can be described as $\tilde{\mathbf{J}} \times \mathbf{B}_0$. The wave equation governing the pressure distribution \tilde{p} can be written as¹¹

$$\nabla^2 \tilde{p} - \frac{1}{c_s^2} \frac{\partial^2 \tilde{p}}{\partial t^2} = \nabla \cdot (\tilde{\mathbf{J}} \times \mathbf{B}_0), \quad (1)$$

where c_s is the acoustic speed in the media. In Eq. (1), $\tilde{\mathbf{J}}(\mathbf{r}, t) = \mathbf{J}(\mathbf{r})\delta(t)$, with an assumption that the induced eddy current has an ideal pulsed distribution over time. This would be a reasonable approximation as long as the excitation coil is sending pulse stimulations that are short enough. Using Green's function, the solution of Eq. (1) can be written as

$$\tilde{p}(\mathbf{r}, t) = -\frac{1}{4\pi} \int_V d\mathbf{r}' \nabla_{\mathbf{r}'} \cdot [\mathbf{J}(\mathbf{r}') \times \mathbf{B}_0(\mathbf{r}')] \frac{\delta(t - R/c_s)}{R}, \quad (2)$$

where $R = |\mathbf{r} - \mathbf{r}'|$ and V is the volume containing the acoustic source. The pressure on a surface surrounding the object can be measured to reconstruct the source term $\nabla \cdot (\mathbf{J} \times \mathbf{B}_0)$ using the time reversing technique^{1,14} as

$$\nabla \cdot (\mathbf{J} \times \mathbf{B}_0) \approx -\frac{1}{2\pi c_s^2} \int_{\Sigma} \int_{\Sigma} dS_d \frac{\mathbf{n} \cdot (\mathbf{r}_d - \mathbf{r})}{|\mathbf{r} - \mathbf{r}_d|^2} \times \tilde{p}''(\mathbf{r}_d, |\mathbf{r} - \mathbf{r}_d|/c_s)/c_s, \quad (3)$$

where \mathbf{r}_d is a point on the detection surface Σ , \mathbf{n} is the normal vector of Σ at \mathbf{r}_d , \mathbf{r} is a point in the object, and the double prime refers to the second derivative over time. In deriving Eq. (3) an item of \tilde{p}' is ignored because it is much smaller than the \tilde{p}'' item in high frequency as around megahertz range.

According to Faraday's law and Ohm's law, we have

$$(\nabla \times \mathbf{J})/\sigma - \nabla \left(\frac{1}{\sigma} \right) \times \mathbf{J} = -\mathbf{B}_1, \quad (4)$$

where \mathbf{B}_1 refers to the space function of the pulsed magnetic field, which has a step function distribution over time according to Faraday's law.¹ For a piecewise homogeneous medium,¹⁵ the conductivity (other than the boundary points) can be calculated as¹

$$\sigma \approx -\frac{(\nabla \times \mathbf{J}) \cdot \mathbf{B}_0}{\mathbf{B}_1 \cdot \mathbf{B}_0}, \quad (5)$$

where $(\nabla \times \mathbf{J}) \cdot \mathbf{B}_0 = \nabla \cdot (\mathbf{J} \times \mathbf{B}_0)$, because of $\nabla \times \mathbf{B}_0 = 0$.

MAT-MI uses pulsed magnetic stimulation and induces a pulsed solenoid electrical field in the object. This induced electrical field can cause high frequency ultrasound waves which enable the MAT-MI approach to obtain a high spatial resolution impedance image. The present phantom study is

^{a)} Author to whom correspondence should be addressed; electronic mail: binhe@umn.edu

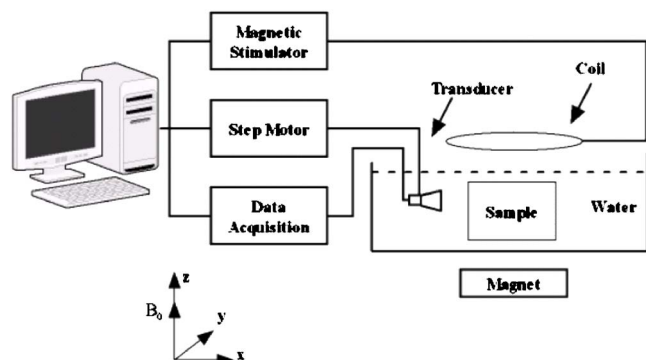


FIG. 1. Diagram of the 2D MAT-MI system setup.

aimed at demonstrating the feasibility of the MAT-MI approach in imaging physiological saline solutions simulating biological tissue.

The diagram of our current experiment setup for MAT-MI is shown in Fig. 1. The magnetic stimulator can send pulsed stimulation (microseconds) through the coil above the sample. The ultrasound sensor driven by the step motor can scan around the sample in a circular orbit. Data acquisition is synchronized with the magnetic stimulation. This composes a two-dimensional (2D) MAT-MI system. Because the reconstruction algorithms shown in (3) and (4) are intrinsic three-dimensional (3D) and require acoustic measurement on a surface surrounding the sample to quantitatively reconstruct the conductivity distribution, this 2D system provides a simplified means of collecting the acoustic signals. However, it is demonstrated that this 2D system can still reconstruct the conductivity boundaries of the sample in the scanning cross section. The reconstruction algorithm thus can be simplified to

$$I(\mathbf{r}) = - \sum_{i=1}^N \frac{\mathbf{r}_i \cdot (\mathbf{r}_i - \mathbf{r})}{|\mathbf{r} - \mathbf{r}_i|^2} \tilde{p}(\mathbf{r}_i, |\mathbf{r} - \mathbf{r}_i|/c_s), \quad (6)$$

where \mathbf{r}_i is the position of the sensor at the i th scanning point and \tilde{p} is the pressure signal after removal of low frequency disturbance by filtering.

In the experimental setup, the pulse width of the stimulation is $0.5 \mu\text{s}$. The radius of the coil is 40 mm. A permanent magnet ($50 \times 50 \times 25 \text{ mm}^3$) is placed 2 cm under the sample and creates a magnetic field of about 0.1 T along the z axis at 2 cm from its surface. The transducer (TC3029, Reson, Inc.) has a central frequency of 500 KHz. The transducer signal is amplified by 80 dB and sampled at 5 MHz. Because of the limited signal-to-noise ratio (SNR), 100 000 times of averaging at the rate of 500 Hz were used.

Reconstructed images of saline samples with different salinities are shown in Fig. 2. The image center is the origin of the scanning circle orbit. The saline samples are put in a plastic cup and emerged in water. This creates a conductivity step which is analog to a homogeneous tissue with higher conductivity embedded in a low conductive one. The transducer scans the sample with a 2.5° step. The right bottom image in Fig. 2 (water sample) indicates that the plastic cup has a little influence on the reconstructed image. It is shown that the current system can distinguish the conductivity dif-

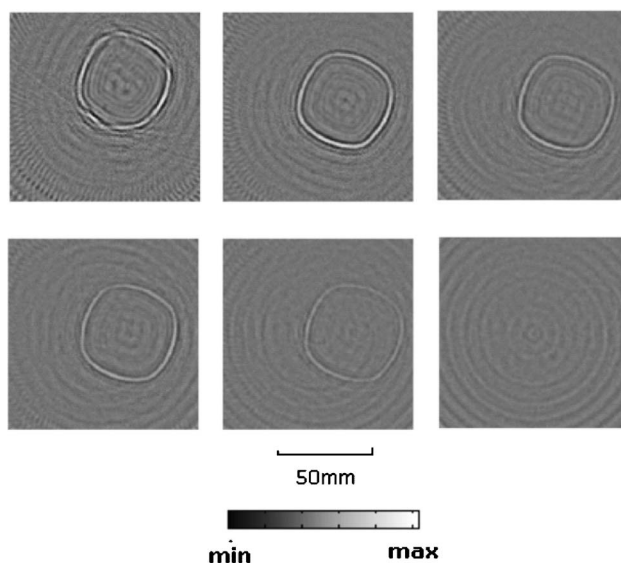
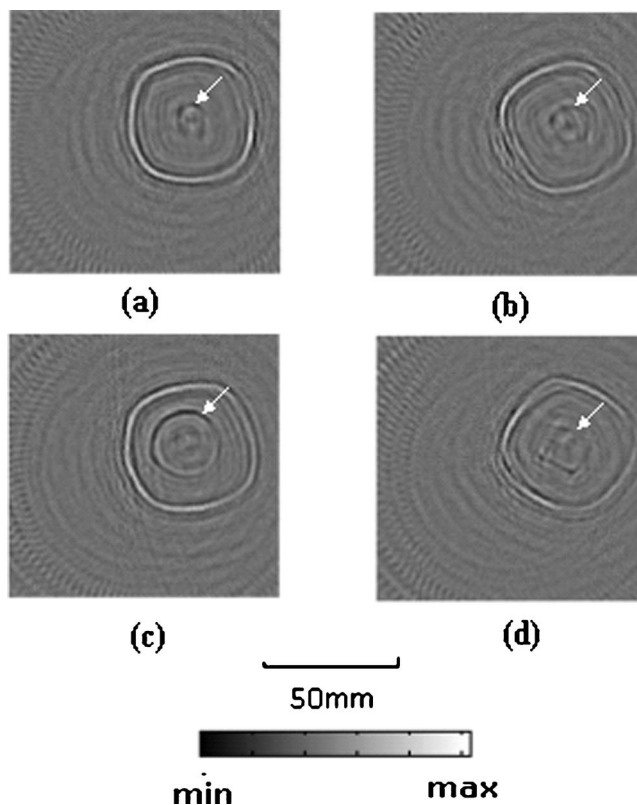


FIG. 2. MAT-MI 2D images of saline samples with different salinities. The salinities are 10%, 8%, 5%, 3%, 1%, and 0% from left to right from top to bottom, respectively.

ference between water and saline samples with salinity of 1%. In addition, it is obvious that the image boundary intensity positively correlated with the salinity thus the conductivity contrast of the sample and background.

Figure 3 shows the reconstructed images of double layer gel phantoms with different inner layer sizes and shapes. The

FIG. 3. MAT-MI 2D images of double layer gel phantoms. The cross section of the inner layer columns are (a) circle with 9 mm diameter, (b) circle with 13 mm diameter, (c) circle with 26 mm diameter, and (d) a square with dimension of 13 mm \times 13 mm, respectively. The reconstructed inner layer conductivity boundaries are marked by white arrows.

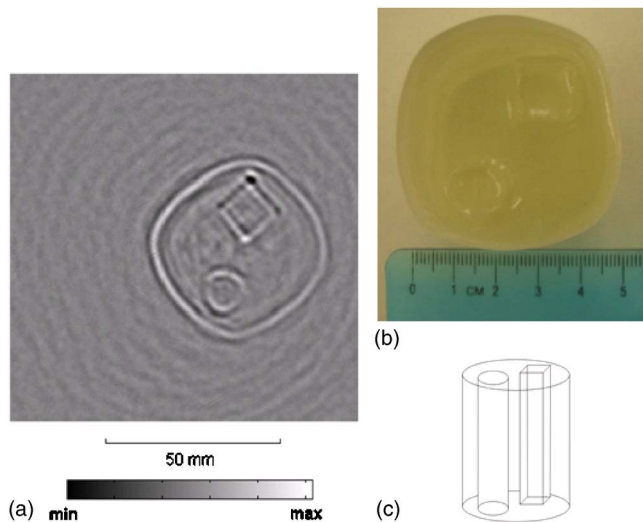


FIG. 4. (Color online) (a) 2D MAT-MI image of a gel phantom with two columns of gels embedded in. (b) Top view photo of the gel phantom. (c) Diagram of the phantom structure.

salinity is 10% for the outer layer and 0% for the inner layer. Plastic film was inserted between the inner layer and outer layer gels to prevent diffusion. The transducer's scanning step is 2.5° . It is shown in Fig. 3 that the shape and size of the conductivity boundaries in the obtained images are consistent with the real sample.

Figure 4 shows another example of the MAT-MI image of a gel phantom. Two columns of gels (a cylinder shape and a square prism shape) with 0% salinity are embedded in gel of 10% salinity with plastic film inserted. The scanning step is 1.25° . As seen in Fig. 4, the 2D MAT-MI image is consistent with the cross section of the phantom in terms of shape and size of the conductivity boundary. In addition, more scanning steps in this case led to a better quality image with less back projection artifacts.

From the current results, it is shown that the width of all the conductivity boundaries in the reconstructed image extends to about 3 mm, indicating an "effective" spatial resolution of 3 mm. Here we define the spatial resolution as the diameter of the smallest structure that can be reconstructed using the current 2D MAT-MI setup. This is partly demonstrated in Fig. 4 that the shortest distance between the inner square prism boundary and the outer layer boundary is

4 mm, which is clearly seen in the reconstructed image. Higher spatial resolution may be obtained by increasing the transducer central frequency and measurement SNR.

The present experiment results from imaging the saline and gel phantoms, which have close conductivity values to those of biological tissue, are promising, demonstrating the feasibility and performance of MAT-MI approach to image electrical impedance of biological tissue with high spatial resolution. Further investigation on 3D MAT-MI system with high signal-to-noise ratio may lead to the establishment of an important noninvasive method for electrical impedance imaging.

In summary, we have demonstrated the MAT-MI approach through a phantom experiment study using the current 2D system. Conductivity boundary images with high spatial resolution have been obtained from saline and gel phantom indicating the feasibility of MAT-MI and its merits for further investigation.

This work was supported in part by NIH RO1EB00178, NSF-BES-0411898, and NSF-BES-0411480 to one of the authors (B.H.), and the Biomedical Engineering Institute of the University of Minnesota.

¹Y. Xu and B. He, *Phys. Med. Biol.* **50**, 5175 (2005).

²K. Paulson, W. Lionheart, and M. Pidcock, *IEEE Trans. Med. Imaging* **12**, 681 (1993).

³P. Metheral, D. C. Barber, R. H. Smallwood, and B. H. Brown, *Nature (London)* **380**, 509 (1996).

⁴J. L. Mueller, D. Isaacson, and J. C. Newell, *IEEE Trans. Biomed. Eng.* **46**, 1379 (1999).

⁵M. Joy, G. Scott, and M. Henkelman, *Magn. Reson. Imaging* **7**, 89 (1989).

⁶O. Kwon, E. Woo, J. Yoon, and J. K. Seo, *IEEE Trans. Biomed. Eng.* **49**, 160 (2002).

⁷N. Gao, S. Zhu, and B. He, *Phys. Med. Biol.* **50**, 2675 (2005).

⁸A. J. Peyton *et al.*, *Meas. Sci. Technol.* **7**, 261 (1996).

⁹H. Griffiths, *Meas. Sci. Technol.* **12**, 1126 (2001).

¹⁰B. C. Towe and M. R. Islam, *IEEE Trans. Biomed. Eng.* **35**, 892 (1988).

¹¹B. J. Roth, P. J. Basser, and J. P. Wikswo, Jr., *IEEE Trans. Biomed. Eng.* **41**, 723 (1994).

¹²H. Wen, J. Shah, and S. Balaban, *IEEE Trans. Biomed. Eng.* **45**, 119 (1998).

¹³H. Wen, *Ultrason. Imaging* **22**, 123 (2000).

¹⁴Y. Xu and L.-H. V. Wang, *Phys. Rev. Lett.* **92**, 033902 (2004).

¹⁵*Modeling and Imaging of Bioelectrical Activity: Principles and Applications*, edited by B. He (Kluwer Academic, Dordrecht, 2004).